nature energy

Article

https://doi.org/10.1038/s41560-024-01681-w

Gradient bandgaps in sulfide kesterite solar cells enable over 13% certified efficiency

Received: 31 March 2024

Accepted: 4 November 2024

Published online: 03 January 2025

Check for updates

Kang Yin[1,2,6], Jinlin Wang[1,2,6], Licheng Lou[1,2,6], Fanqi Meng[3,6], Xiao Xu[1,2], Bowen Zhang[1,2], Menghan Jiao[1,2], Jiangjian Shi[1] ✉, Dongmei Li[1,2,4], Huijue Wu[1], Yanhong Luo[1,2,4] ✉ & Qingbo Meng[1,2,4,5] ✉

Sulfide kesterite Cu_2ZnSnS_4 (CZTS)—a non-toxic and low-cost photovoltaic material—has always faced severe charge recombination and poor carrier transport, resulting in its cell efficiency record stagnating at around 11% for years. The implementation of gradient bandgaps is a promising approach to relieving these issues, but it has not been effectively realized in kesterite solar cells due to challenges around controlling the elemental distribution. Here, based on Cd-alloyed CZTS, we propose a pre-crystallization strategy to reduce the intense vertical mass transport and Cd rapid diffusion in the film growth process, thereby realizing a Cd-gradient CZTS absorber. This absorber, exhibiting a downward-bent conduction band structure, effectively enhances the bulk carrier transport and additionally improves the interface properties of the CZTS/CdS heterojunction. These benefits significantly enhance the photoelectric conversion performance of the cell and help in achieving a certified total-area cell efficiency of about 13.2% with obviously reduced voltage loss, realizing a substantial step forward for the pure-sulfide kesterite solar cell.

Kesterite $Cu_2ZnSn(S,Se)_4$ (CZTSSe) thin-film solar cells have attracted extensive attention in recent years due to their environmental friendliness, low cost and high stability[1–5]. In particular, Se-based kesterite cells have achieved a power conversion efficiency (PCE) close to 15%[6], demonstrating promising application of these material systems. Pure-sulfide Cu_2ZnSnS_4 (CZTS) is an important branch of kesterite materials. The bandgap of CZTS can be easily adjusted within a wide range of 1.3–2.1 eV through the alloying of metal elements (Cd, Ge or Ag)[7–10]. This tunability makes CZTS highly suitable not only for single-junction solar cells but also the uppermost cells for tandem cell stacks[3]. However, despite numerous research efforts over recent years[3,7,11,12], the photoelectric performance of pure-sulfide kesterite cells still faces major bottlenecks, with certified efficiencies remaining stagnate at around 11% for several years[3,13]. The main limitation lies in the low open-circuit voltage (V_{OC})[14–17], with the highest reported value only reaching ~63% of its theoretical Shockley–Queisser limit (V_{OC}^{SQ}) until now[9].

Theoretical studies have shown that deep defects in CZTS materials, such as SnZn and Vs–CuZn, have extremely large electron capture cross-sections (10^{-12} cm^2) due to the strong electron–phonon coupling[16,18]. In addition, compared with CZTSe, CZTS has a higher electron effective mass and thus a lower charge transport ability[19,20]. Moreover, the high-temperature sulfurization process for CZTS often introduces significant Cu/Zn disorder, also inducing the formation of high-concentration deep defects[15,21–23]. The presence of Cu/Zn disorder and deep defects leads to energy band and potential fluctuations, which further increase charge transport scattering and diminish charge transport performance[24,25]. These intrinsic semiconductor properties of CZTS materials pose challenges for charge transport

[1]Beijing National Laboratory for Condensed Matter Physics, Renewable Energy Laboratory, Institute of Physics, Chinese Academy of Sciences, Beijing, People's Republic of China. [2]School of Physical Sciences, University of Chinese Academy of Sciences, Beijing, People's Republic of China. [3]School of Materials Science and Engineering, Peking University, Beijing, People's Republic of China. [4]Songshan Lake Materials Laboratory, Dongguan, People's Republic of China. [5]Center of Materials Science and Optoelectronics Engineering, University of Chinese Academy of Sciences, Beijing, People's Republic of China. [6]These authors contributed equally: Kang Yin, Jinlin Wang, Licheng Lou, Fanqi Meng. ✉e-mail: shijj@iphy.ac.cn; yhluo@iphy.ac.cn; qbmeng@iphy.ac.cn

and defect control, consequently limiting further enhancement of device performance.

The construction of gradient conduction band structure within the absorber is considered to be a promising approach to improve the transport ability of minority carriers over a large spatial scale, thus minimizing non-radiative charge recombination loss[26–28]. The gradient bandgap strategy has obtained wide success in Cu(In,Ga)Se_2 (CIGS) solar cells[26,27], but still encounters challenges in kesterite solar cells, despite extensive efforts. For example, Wu et al.[29] attempted to fabricate an Ag gradient-alloyed CZTSSe film. However, Ag diffusion and gradient distribution is difficult to control at high temperatures and Ag alloying is not effective in controlling the conduction band structure[30]. Researchers have also explored introducing an S/Se gradient into the kesterite absorber[31–33], although the different melting points and reaction activities of Se and S pose challenge in achieving precise control of the S/Se ratio and spatial distribution during the complex selenization (sulfurization) process[4,31,34,35]. Cd gradients have also been observed in kesterite cells. It was found that heterojunction annealing can induce Zn/Cd interdiffusion, resulting in a slight Cd gradient on the surface of the kesterite absorber[36]. Although Cd alloying can lower the conduction band position of kesterite[3,7,30], the heterojunction annealing-induced gradient distribution is insufficient to construct an effective gradient bandgap at a sub-micrometre scale. Therefore, the construction of a gradient conduction band in CZTS absorbers remains a significant challenge in this field, but it is also a direction in which we must continue to make efforts.

In this work, we proposed a pre-crystallization strategy involving Cd alloying to successfully achieve gradient bandgap engineering for solution-processed CZTS. On the one hand, the pre-crystallization strategy induces homogeneous nucleation within the CZTS film and thus reduces the intense vertical mass transport during the film growth process. On the other hand, it improves the initial crystal quality of CZTS, thus increasing the diffusion barriers of Cd. These collective effects enable a significant Cd gradient to be realized in the CZTS absorber. Cd-gradient CZTS exhibits a conduction band-dominated gradient bandgap with effective promotion of carrier transport. Additionally, the Cd-rich CZTS surface improves conduction band alignment of kesterite/CdS and reduces the interface defect. With these benefits, we achieved a certified total-area cell efficiency of 13.16% and significantly reduced V_{OC} loss compared with previously reported results[9,37]. These outcomes represent a substantial step forward for pure-sulfide kesterite solar cells.

Pre-crystallization to form a Cd-gradient CZTS absorber

Cd as an alloying element in pure-sulfide CZTS materials shows great potential for achieving a gradient bandgap. First, the bandgap of Cd-alloyed CZTS changes linearly with the Cd/(Cd + Zn) ratio, ranging from 0–0.4 (refs. 38–40). Second, Cd-alloyed CZTS can effectively suppress Cu/Zn disorder and improve crystal quality, resulting in good photoelectric performance over a wide range of Cd substitutions[3,8,10,12,41,42]. Third, the incorporation of Cd in CZTS can theoretically regulate the conduction band position, thus enabling the realization of a conduction band gradient design and modifying the unfavourable conduction band energy alignment of the CZTS/CdS heterojunction[3,7,30]. Based on these foundations, the primary focus of our work was to achieve a gradient distribution of Cd in the CZTS.

In our experimental approach, precursor solutions of CZTS and Cu_2CdSnS_4 (CCTS) were prepared separately for sequential deposition of the CZTS and CCTS precursor layers onto the Mo substrate, obtaining a Mo/CZTS/CCTS precursor film. To address the issue related to rapid interdiffusion of Zn/Cd in the high-temperature sulfurization process, we proposed the introduction of a pre-crystallization process (as depicted in Fig. 1a). This pre-crystallization was carried out by pre-annealing the dual-layer precursor film at 420 °C for 10 min under a H_2S (10%)/Ar atmosphere. Afterwards, the pre-crystallized film was sulfurized with the aid of S powder under high temperatures. To elucidate the influence of H_2S pre-crystallization on the film and the following sulfurization process, we conducted microstructure and elemental chemical state investigations of the pre-crystallized film. The results revealed that this process could effectively eliminate the organic components and metal–oxygen coordination from the film while introducing more pronounced metal–S coordination (Supplementary Figs. 1 and 2). The high reactivity of H_2S at high temperature, together with strong metal–S interaction, is the possible reaction mechanism for this phenomenon (Supplementary Note 1). This change helped the entire film to obtain homogeneous nucleation along the vertical direction. In Fig. 1b, lattice structures, along with their fast Fourier transform patterns, can be clearly seen in different vertical regions of the pre-crystallized film. Particularly, these regions exhibited similar fast Fourier transform patterns, indicating that they have identical crystal phase and crystallization qualities. This was significantly different from the film only pre-annealed under an atmosphere of N_2, which exhibited more pronounced organic residues, a more pronounced amorphous phase and an obviously lower crystallization quality (Supplementary Fig. 3).

In the subsequent sulfurization process, the sample without pre-crystallization exhibited preferential crystallization in the top region, whereas amorphous or disordered phases were still very significant in the bottom region (Fig. 1c and Supplementary Fig. 4). With sulfurization proceeding, upper grains rapidly merged into larger crystals and engulfed fine crystals beneath them, leading to the formation of numerous voids at the bottom of the final absorber (Supplementary Fig. 5). This process was usually accompanied by intense elemental interdiffusion, causing the initial Zn/Cd gradient to rapidly decline and eventually disappear during the sulfurization process (Fig. 1d,e). In contrast, the pre-crystallized sample exhibited uniform nucleation and crystal growth throughout the film, in which ordered lattice fringes could be seen clearly in different regions along the vertical direction (Fig. 1c). The homogeneous nucleation and crystal growth improved the film morphology and additionally diminished the driving force for elemental interdiffusion, thus allowing the Zn/Cd element gradient to be retained until the end of the sulfurization process (Fig. 1d,e and Supplementary Figs. 6 and 7).

Raman measurements were employed to characterize the influence of elemental interdiffusion on the CZTS phase formation process. Due to the interdiffusion-induced elemental composition change, the Raman spectra—especially the peak position of the kesterite phase—exhibited obvious evolution during the sulfurization process (Supplementary Fig. 8). Specifically, the Raman peaks of both samples blue shifted continuously as sulfurization proceeded (Fig. 1f), indicating gradual upward diffusion of Zn towards the CCTS layer. The Raman peak of the sample without pre-crystallization showed a rapid shift in the initial stage and remained almost constant after 9 min of sulfurization, indicating completion of Zn/Cd interdiffusion. Comparatively, the Raman peaks of the pre-crystallized sample exhibited a slower shift and did not reach equilibrium, even when sulfurization ended. For the final state, the pre-crystallized sample possessed a lower-wavenumber Raman peak than the control sample, indicating higher Cd content. These results demonstrate that pre-crystallization effectively impeded the interdiffusion of Zn/Cd elements, thus enabling the realization of an element gradient.

In addition to diminishing the driving force of element diffusion through homogeneous nucleation growth, the improvement of film crystal quality induced by H_2S pre-crystallization is also an important reason for reduced Zn/Cd interdiffusion. In the absence of pre-crystallization, the film usually undergoes surface nucleation and top-down crystal growth[4,34]. This growth mode is accompanied by a rapid upward diffusion of elements at the onset of reaction, resulting in local lattice distortion and atomic vacancies (Supplementary Fig. 9).

https://doi.org/10.1038/s41560-024-01681-w

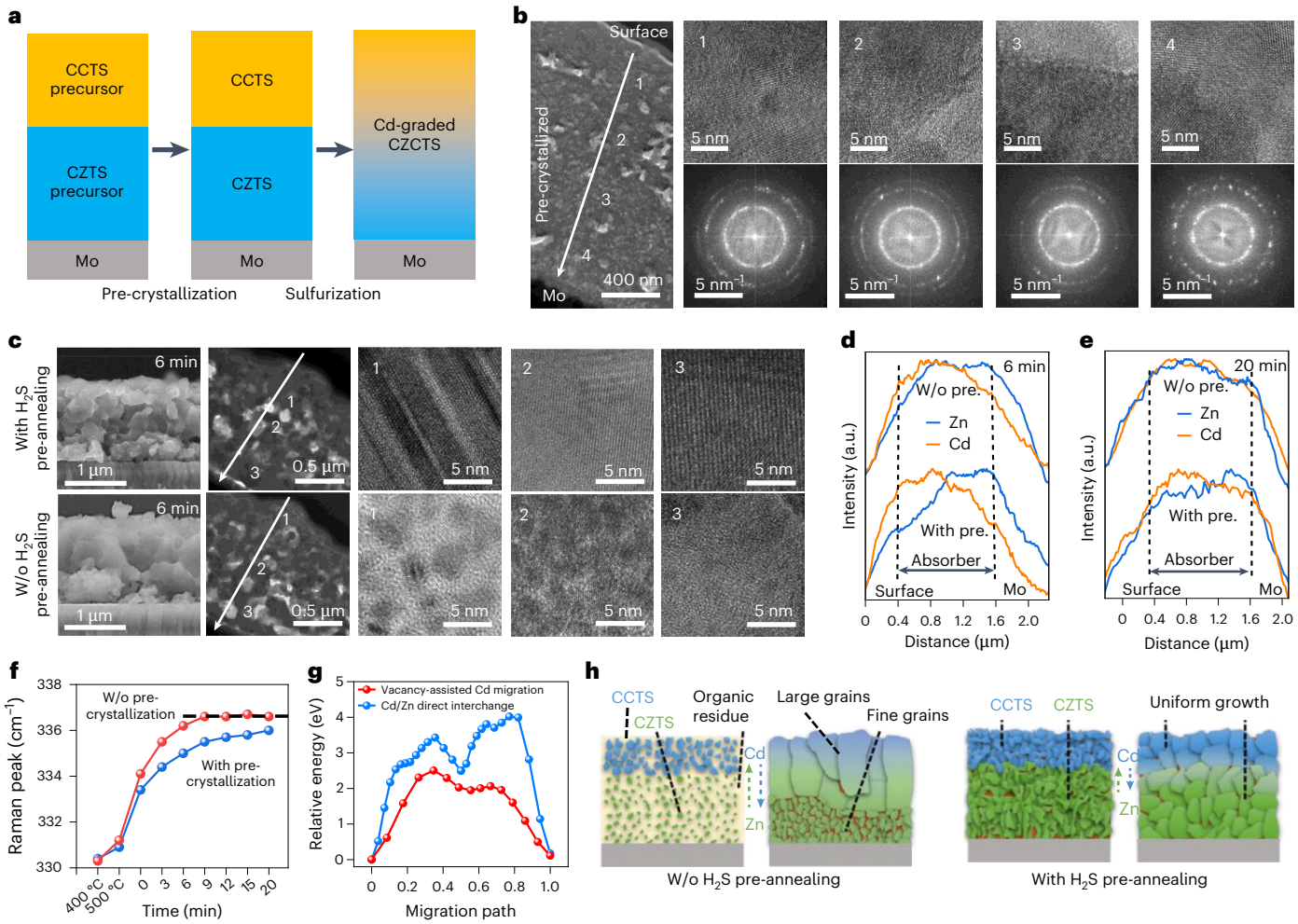

Fig. 1 | Influence of pre-crystallization on the sulfurization process. **a**, Schematic of the process used to prepare the Cd-gradient CZTS absorber through pre-crystallization and subsequent sulfurization. **b**, Cross-sectional transmission electron microscopy images of the pre-crystallized sample and fast Fourier transform patterns transformed from the atomic images captured in different regions. **c**, Cross-sectional scanning electron microscopy and transmission electron microscopy images of the Cd-CZTS films after sulfurization for 6 min with and without pre-crystallization. The white arrows depict the direction from the surface to the substrate. **d**,**e**, Normalized scanning electron microscopy with energy-dispersive X-ray analysis elemental profiles of the films sulfurized for 6 (**d**) and 20 min (**e**). The vertical dashed lines are guidance for the eyes, depicting the surface and substrate of the film. **f**, Raman peak evolution of the CZTS phases of the two samples (with and without pre-crystallization) at different sulfurization stages (532 nm excitation). The dashed line is guidance for the eyes. **g**, Calculated relative energies of the Zn/Cd interchange as a function of the migration path through direct versus vacancy-assisted mechanisms. **h**, Schematic of the grain growth process of the film without (left) versus with the pre-crystallization process (right). pre., pre-annealing; w/o, without.

In contrast, owing to the previous removal of organic residues and the initiation of homogeneous nucleation in advance, pre-crystallized samples exhibit much improved lattice ordering. In this case, the exchange of Zn/Cd mainly transpires at the CCTS/CZTS interface with a gentler process. To provide further clarity, we employed density functional theory (DFT) calculations to compare the energy barriers for Zn/Cd interchange in the kesterite lattice through direct or vacancy-assisted mechanisms (Supplementary Fig. 10). The results (Fig. 1g) indicated that in order to sustain the high diffusion barrier, the vacancy path in the lattice needs be eliminated, which thus highlighted the significance of enhancing the quality of the initial crystals in the film, as realized by the pre-crystallization process. For clarity, schematics of these two different grain growth processes are shown in Fig. 1h.

Notably, besides the gradient composition, other positive effects caused by the Cd alloying itself, such as promoting crystallization, inhibiting formation of the ZnS secondary phase, minimizing Sn loss during sulfurization and reducing Cu/Zn disorder, were also observed in our experiment (Supplementary Figs. 11–13). These effects could be important reasons for the cell performance improvement through Cd alloying[8,12]. Comparatively, the effects of H_2S pre-crystallization itself on defect concentration, charge trapping activity and film morphology were far less significant than those of Cd elemental involvement, either via homogeneous or gradient alloying. These results suggest that the primary role of H_2S pre-crystallization lies in realizing gradient Cd in the absorber film.

Elemental composition and energy band characteristics

We used scanning transmission electron microscopy (STEM) and high-angle annular dark field (HAADF) imaging to further quantitatively investigate the distribution of Zn/Cd in the Cd-gradient CZTS (GCd-CZTS) absorber. As in Fig. 2a and Supplementary Fig. 4, the cross-sectional STEM image exhibited uniform HAADF contrast across the entire film, with large grains. The film also showed clear selected-area electron diffraction patterns corresponding to the [221] observation direction of the kesterite lattice (Supplementary Fig. 14a). These results demonstrated a high crystallization quality of the fabricated GCd-CZTS absorber. HAADF atomic images of the film were

https://doi.org/10.1038/s41560-024-01681-w

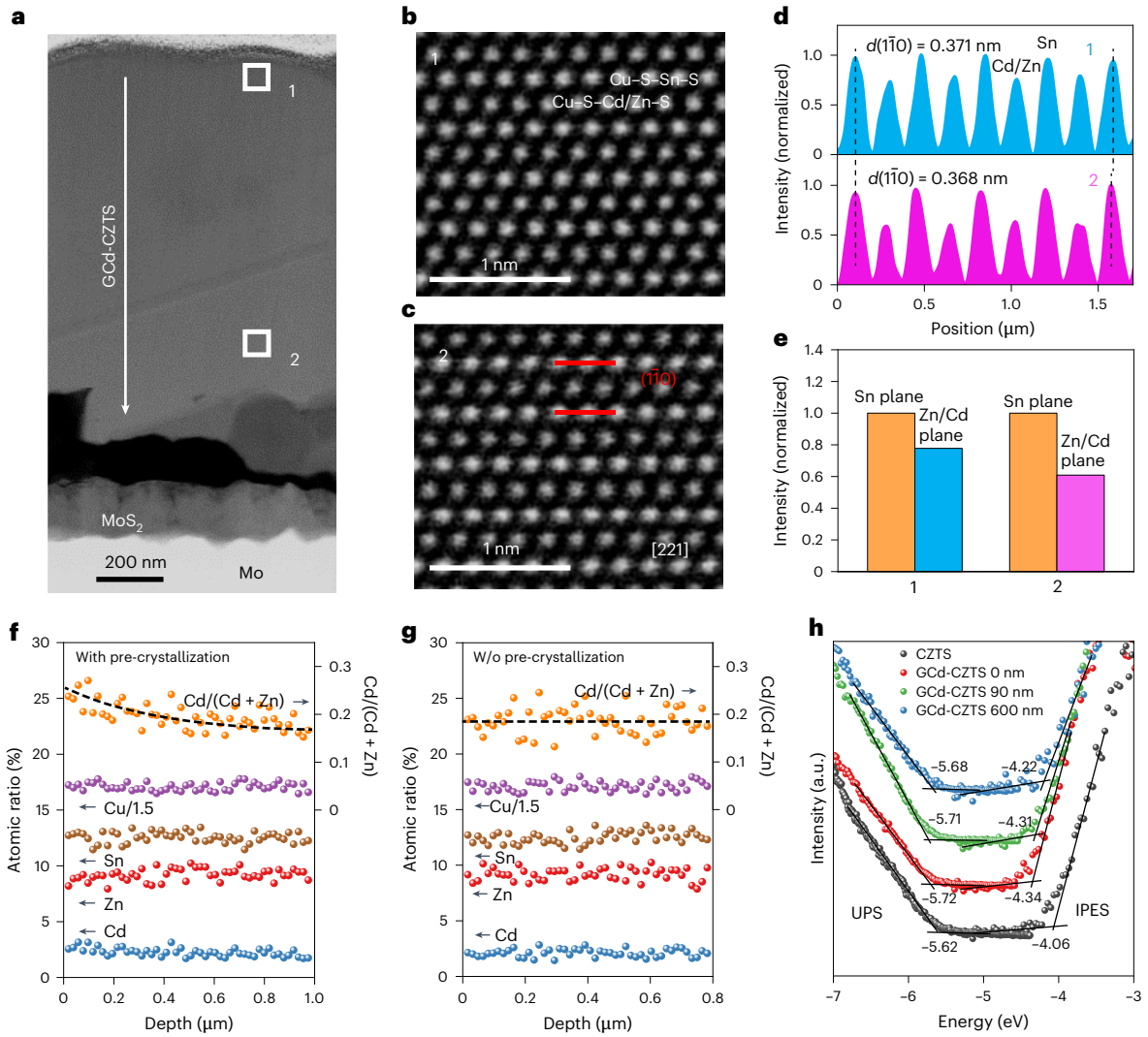

Fig. 2 | Elemental and energy band gradients. a, Cross-sectional HAADF STEM image of the GCd-CZTS sample. **b**,**c**, Filtered HAADF atomic images taken from regions 1 (**b**) and 2 (**c**) in the film. **d**,**e**, Averaged intensity profiles of the (1$\bar{1}$0) plane (**d**) and normalized total intensities of the Sn and Zn/Cd planes (**e**) from the atomic images of regions 1 and 2. **f**,**g**, STEM with energy-dispersive X-ray analysis of the elemental distribution in the films with (**f**) or without pre-crystallization (**g**). This was performed along the white line, as marked in the STEM image. The dashed lines are guidance for the eyes. **h**, UPS and inverse photoelectron spectroscopy (IPES) spectra of CZTS and GCd-CZTS absorbers (with etching depths of 0, 90 or 600 nm). The positions of the valence band maximum and conduction band minimum of these samples were determined as the intersection between the background and the signal onset (solid black lines).

further captured (Fig. 2b,c), in which the top and bottom regions showed the same atomic arrangements. Along the [1$\bar{1}$0] direction, alternate arrangements of light and dark contrast corresponding to Cu–Sn and Cu–Zn/Cd planes could be clearly observed (Supplementary Fig. 14b). In Fig. 2d,e, quantification of the averaged HAADF contract profiles revealed that the (1$\bar{1}$0) interplanar spacing of region 1 in the top of the film was 0.371 nm, which was slightly larger than that of region 2. Moreover, when using the HAADF intensity of the Cu–Sn plane as a reference, the Cu–Zn/Cd plane of region 1 showed an obviously higher intensity than that of region 2, indicating a much larger averaged atomic number (that is, more Cd in the kesterite lattice of the top region).

The Zn/Cd distribution in the GCd-CZTS film was further determined by STEM with energy-dispersive X-ray analysis measurement. As in Fig. 2f, the Cd/(Cd + Zn) ratio exhibited a gradient distribution across the absorber film, exceeding 0.26 in the surface region and gradually decreasing to ~0.16 at the back interface. In contrast, in the sample without pre-crystallization, all elements exhibited uniform distribution, and no gradient in the Cd/(Cd + Zn) ratio was observed (Fig. 2g and Supplementary Fig. 15). These results agree well with the scanning electron microscopy with energy-dispersive X-ray analysis and secondary ion mass spectrometry measurements (Fig. 1e and Supplementary Figs. 5 and 6). We further measured the Cd/(Cd + Zn) ratio-dependent energy band properties of Cd-alloyed CZTS materials using ultraviolet photoelectron spectroscopy (UPS), Kelvin probe force microscopy (KPFM) and external quantum efficiency (EQE) spectra. According to the measured Zn/Cd distribution in the GCd-CZTS absorber, a gradient bandgap structure was observed (Supplementary Fig. 16). In addition, it was also found that a spike energy band alignment was formed at the heterojunction interface, which would help to reduce the interfacial charge recombination.

We also used UPS and inverse photoelectron spectroscopy to more directly determine the energy band structures of the GCd-CZTS absorber (Fig. 2h). For the film surface, the positions of the valence band maximum and conduction band minimum (CBM) were determined at −5.72 and −4.34 eV, respectively, corresponding to a bandgap of 1.38 eV. Compared with the pure CZTS, the downward shift of the CBM reached 280 meV. Through mechanical etching, the energy band properties of the GCd-CZTS absorber at 90 and 600 nm depths

were also measured. Figure 2h shows that moving deeper into the film the CBM of the absorber exhibited an obvious upward shift and approached −4.22 eV at 600 nm. This result revealed that the gradient of the CBM between the surface and the lower region of the GCd-CZTS absorber reached 120 meV, thus confirming the formation of effective gradient band structures, which should be able to facilitate electron transport.

Photoelectric characterization of the film and device

We further characterized the influence of gradient band structure on the carrier transfer characteristics of the absorber using emission wavelength-dependent time-resolved photoluminescence spectroscopy (Fig. 3a–c)[43]. For clarity, the times of the photoluminescence maxima at different wavelengths are marked out by black lines in Fig. 3a,b and the transient photoluminescences probed at short and long wavelength are shown in Fig. 3c (880 and 975 nm for CZTS and 920 and 1,025 nm for GCd-CZTS). The emission of GCd-CZTS at 920 nm exhibited a sharp drop behaviour in the early stage, whereas the emission at 1,025 nm rose slowly. A time delay of about 4 ns was observed between these two emission bands. Matching of the dynamics between the 920-nm-emission decay and the concomitant rise of the 1,025 nm emission implied ultrafast carrier transfer between these two emission states. This phenomenon strongly supports gradient-band-structure-driven fast carrier transfer within the absorber, which will help to reduce the recombination loss of photogenerated carriers in the bulk absorber during the transport process. Comparatively, no such behaviour was observed in the gradient-free CZTS sample.

In addition to confirming fast carrier transfer, we also investigated the surface electric and defect properties of these films using KPFM. As in Fig. 3d, the contact potential difference distribution of the GCd-CZTS sample was barely influenced by the measurement conditions (dark versus illumination), indicating negligible surface defect and charge trapping behaviours. Comparatively, the averaged contact potential difference of the pure CZTS sample shifted by about 26 mV under light illumination due to defect-charge-trapping-induced energy band bending[4]. These results were further supported by a direct measurement of charge distribution within the absorbers using drive-level capacitance profiling and capacitance–voltage (C–V) methods[44] (Fig. 3e). By calculating the charge density difference between these two methods, the interfacial defect density of the GCd-CZTS sample (8.1×10^{15} cm^{-3}) was found to be nearly one order of magnitude lower than that of the CZTS sample (6.9×10^{16} cm^{-3}). Additionally, the GCd-CZTS sample showed a much lower bulk charge density, indicating a decrease in the defect concentration through Cd alloying. This consequently increased the depletion width of the absorber, which would facilitate carrier transport in a larger spatial region. In the capacitance–frequency spectra (Supplementary Fig. 13), such a difference in the defect response could also be observed. For the samples incorporating Cd (whether through gradient or homogeneous alloying), the low-frequency defect capacitance was much smaller than that of the control CZTS sample. This defect has a relatively wide frequency response distribution and does not seem to be a Gaussian-type defect. Therefore, we speculate that it may be the charge trapping/detrapping response due to the band or potential fluctuations caused by deep defects. That is, the Cd alloying effectively reduces the band or potential fluctuations of the kesterite absorber, in line with the results observed before[12,45]. Due to these benefits, for the temperature-dependent V_{OC} measurement, the difference between the charge recombination energy barrier (E_A) and bandgap (E_g) of the fabricated GCd-CZTS cell ($E_g - E_A$) was much smaller than that of the CZTS solar cell[46] (Fig. 3f) (that is, there was much less voltage loss).

We further used a modulated transient photocurrent to investigate the overall charge transport and charge loss characteristics of the fabricated cells (Fig. 3g–i). With the improved energy band structure and facilitated carrier transport, the GCd-CZTS device exhibited a much smaller photocurrent decay time. In addition, the photocurrent peak intensity of this device exhibited a smaller decline compared w that of the control CZTS device as the bias voltage increased, implying more efficient and more stable carrier extraction from the absorber to the buffer/window layers. Together with the photovoltage decay properties (Supplementary Fig. 17), the charge extraction (η_e) and collection (η_c) efficiencies—reflecting the charge loss in the bulk and interface regions of the cells, respectively—were quantified[47,48]. It is apparent that the GCd-CZTS cell possessed much higher η_e in the entire voltage range (that is, a much lower bulk charge loss primarily resulting from gradient-bandgap-enhanced bulk carrier transport). The GCd-CZTS cell also showed higher η_c at high voltages of >0.5 V (that is, lower charge loss caused by interface charge recombination).

Device performance

For solar cell fabrication, we further optimized the sulfur source in the entire reaction processes and the precursor CCTS/CZTS ratio. We confirmed that the best device performance could be obtained by using H_2S and S powders as the sulfur sources in the pre-crystallization and subsequent sulfurization processes, respectively (Supplementary Figs. 18 and 19). For precursor composition optimization (Supplementary Fig. 20), we found that a PCE higher than 13% could be obtained at a wide range of CCTS/CZTS ratios, from 0.17–0.38, although these cells exhibited different performance parameters (Fig. 4a). Specifically, a ratio of 0.17 resulted in cells with the highest V_{OC}, whereas a ratio of 0.38 resulted in cells exhibiting higher short-circuit current density (J_{SC}) and fill factor (FF). This wide composition window makes our strategy very feasible in experiments. One of our cells fabricated with a CCTS/CZTS ratio at 0.38 was sent out to an independent laboratory (the National PV Industry Measurement and Testing Center) for certification. As in Fig. 4b, the certified total-area PCE of the cell reached 13.16% (Supplementary Fig. 21). When operating continuously at the maximum power point of 581.8 mV, the cell gave a constant current output of 22.67 mA cm^{-2}, confirming a certified steady-state PCE of slightly more than 13.19% (Fig. 4c). Compared with previously reported results[9,13,49], our cell has achieved significant efficiency enhancement and V_{OC} loss reduction, thus representing a substantial step forward for the pure-sulfide kesterite solar cell.

To demonstrate the beneficial effect of gradient energy band structure, we further make a comparison with cells based on homogeneous Cd alloying (Fig. 4d and Supplementary Figs. 22 and 23). For cells based on homogeneous Cd alloying without adoption of the pre-crystallization strategy, the highest averaged total-area PCE was only 11.3% at a Cd/(Cd + Zn) ratio of 40%, which is comparable to that of gradient-Cd cells also without adoption of the pre-crystallization process. After adopting the pre-crystallization strategy, the averaged PCE of the cells based on homogeneous Cd alloying was a little improved (12%). A similar small degree of PCE improvement (by ~0.5%) arising from the pre-crystallization itself was also observed in the Cd-free CZTS cells, probably due to the slightly reduced ZnS secondary phase on the film surface (Supplementary Fig. 24). Overall, these comparative results indicate that only by synergistically utilizing gradient-Cd and pre-crystallization strategies to construct gradient bandgap structure can the cell performance be effectively improved to exceed 13%. Notably, the better back contact observed in the GCd-CZTS sample (Supplementary Fig. 12) may have also contributed to the cell performance improvement through facilitating hole transport at the GCd-CZTS/Mo interface. Nonetheless, we also need to note that the extent to which the improvement in contact morphology affects final cell performance remains uncertain because it also provides a pathway for electron backward transfer, causing charge loss.

We further investigated the voltage deficits of these cells by comparing the cell V_{OC} values with their theoretical limits[18]. The representative current–voltage curves of the highly efficient GCd-CZTS solar cells

https://doi.org/10.1038/s41560-024-01681-w

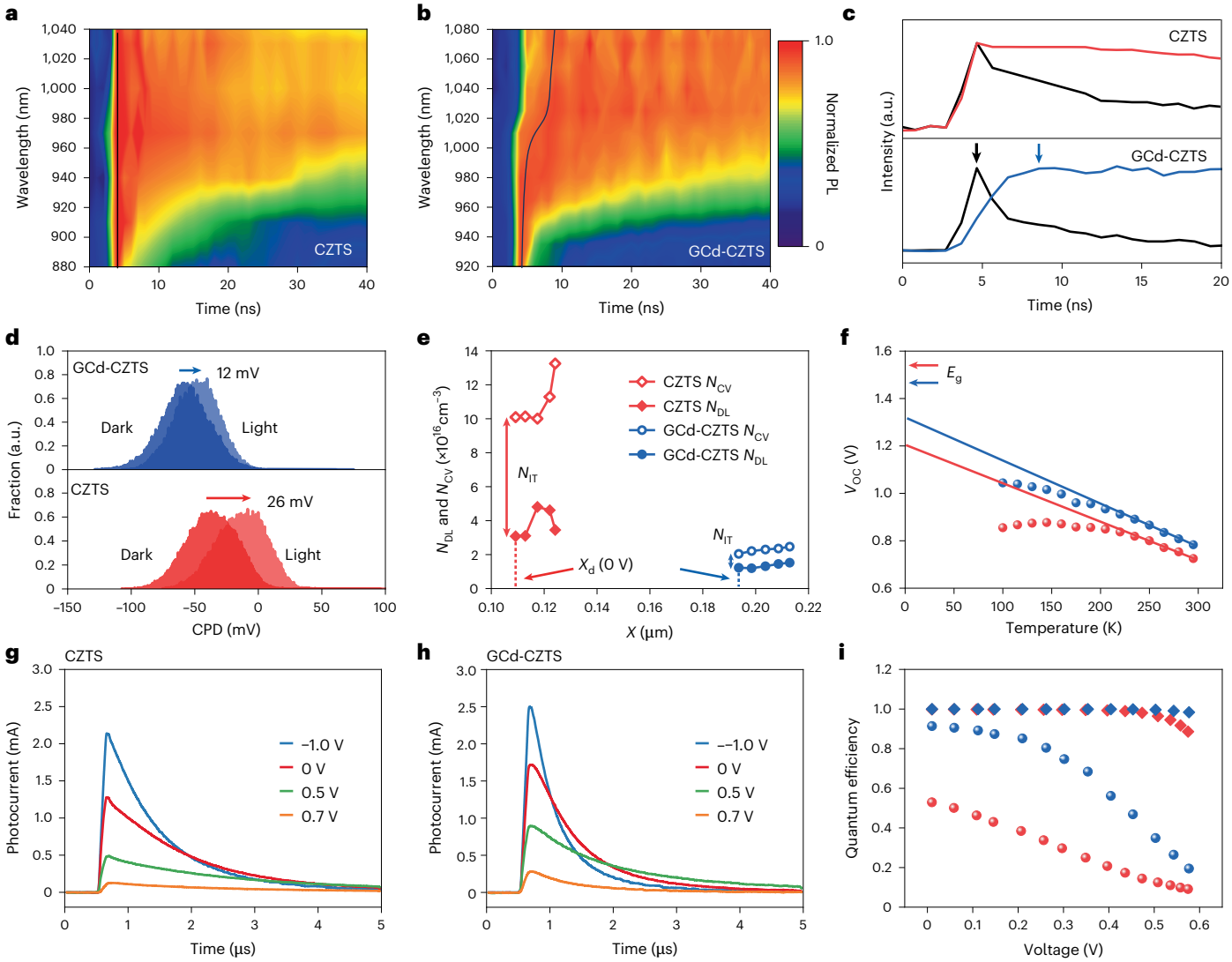

Fig. 3 | Photoelectric characterization of the film and device. a,**b**, Two-dimensional pseudocolour plots of transient photoluminescence (PL) as functions of emission wavelength and time delay for the CZTS and GCd-CZTS films (40 K; excitation at 640 nm). The black lines mark the times of the photoluminescence maxima at different wavelengths. **c**, Time-resolved photoluminescence decay at different emission wavelengths (880 (black) and 975 nm (red) for CZTS and 920 (black) and 1,025 nm (blue) for GCd-CZTS). The arrows show the time delays of the different emissions of the GCd-CZTS sample. **d**, Contact potential difference (CPD) distribution of the CZTS and GCd-CZTS samples in the dark and under illumination. **e**, Charge profiles of the CZTS and GCd-CZTS cells obtained by drive-level capacitance profiling (N_{DL}) and capacitance–voltage (N_{CV}) methods (measured at 3 kHz). The vertical dashed lines are guidance for the eyes and the vertical arrows depict the differences between N_{DL} and N_{CV} (N_{IT}). **f**, Temperature-dependent V_{OC} values of the CZTS (red) and GCd-CZTS devices (blue). The solid lines are the linear fits of the data points in the high-temperature region. The charge recombination energy barriers (E_A) were 1.20 and 1.31 eV, respectively, and the bandgaps (E_g; arrows) were 1.54 and 1.45 eV, respectively. **g**,**h**, Photocurrent decay behaviours of the CZTS (**g**) and GCd-CZTS cells (**h**) under various bias voltages. The exponential decay times were 0.88, 1.34, 2.14 and 2.04 μs (**g**) and 0.48, 0.81, 1.41 and 1.23 μs (**h**) for −1.0, 0, 0.5 and 0.7 V, respectively). **i**, Charge collection (η_c; diamonds) and extraction efficiencies (η_e; circles) of the CZTS (red) and GCd-CZTS cells (blue), derived from modulated electrical transient measurements.

are given in Fig. 4e. For the cell with a CCTS/CZTS ratio of 0.17, the V_{OC} reached 805 mV, which exceeds values reported for sulfide kesterite solar cells with a bandgap of <1.6 eV (refs. 9,49). From the EQE spectra, the effective bandgaps of the GCd-CZTS absorbers in these three cells with CCTS/CZTS ratio of 0.17, 0.25 and 0.38 were determined to be 1.45, 1.42 and 1.37 eV, respectively (Fig. 4f and Supplementary Fig. 25). As calculated and shown in Fig. 4g, the V_{OC}/V_{OC}^{SQ} values of these cells all exceeded 65% and the best-performing cell reached 67.9%, surpassing the reported result of 63.2% obtained in a Ge-alloyed and gradient-free CZTS solar cell[9]. We also performed additional third-party certification on the high-bandgap solar cells to confirm this impressively high V_{OC}/V_{OC}^{SQ}, which finally obtained a verified high value of 67.0%. This result is even higher than that obtained in CZTSSe solar cells with a PCE of >14.5%[45,50], thus demonstrating the significant effect of the gradient bandgap in reducing the voltage loss of kesterite solar cells.

Moreover, our strategy exploits the energy band and crystallization regulation effect of Cd, thus providing a promising path for achieving high-performance kesterite devices through low-content Cd alloying (for example, <20%). In addition to the sulfide kesterite cell, the pre-crystallization strategy that works primarily through homogeneous nucleation crystallization and enhancement of the initial crystal quality is also insightful for the construction of an effective gradient bandgap in significantly thinned CIGS and CdSe/CdTe solar cells. The high reaction activity of H_2S also provides more routes by which to remove organic residues in the kesterite precursor film that were introduced from organic solvents and ligands. This will help to

https://doi.org/10.1038/s41560-024-01681-w

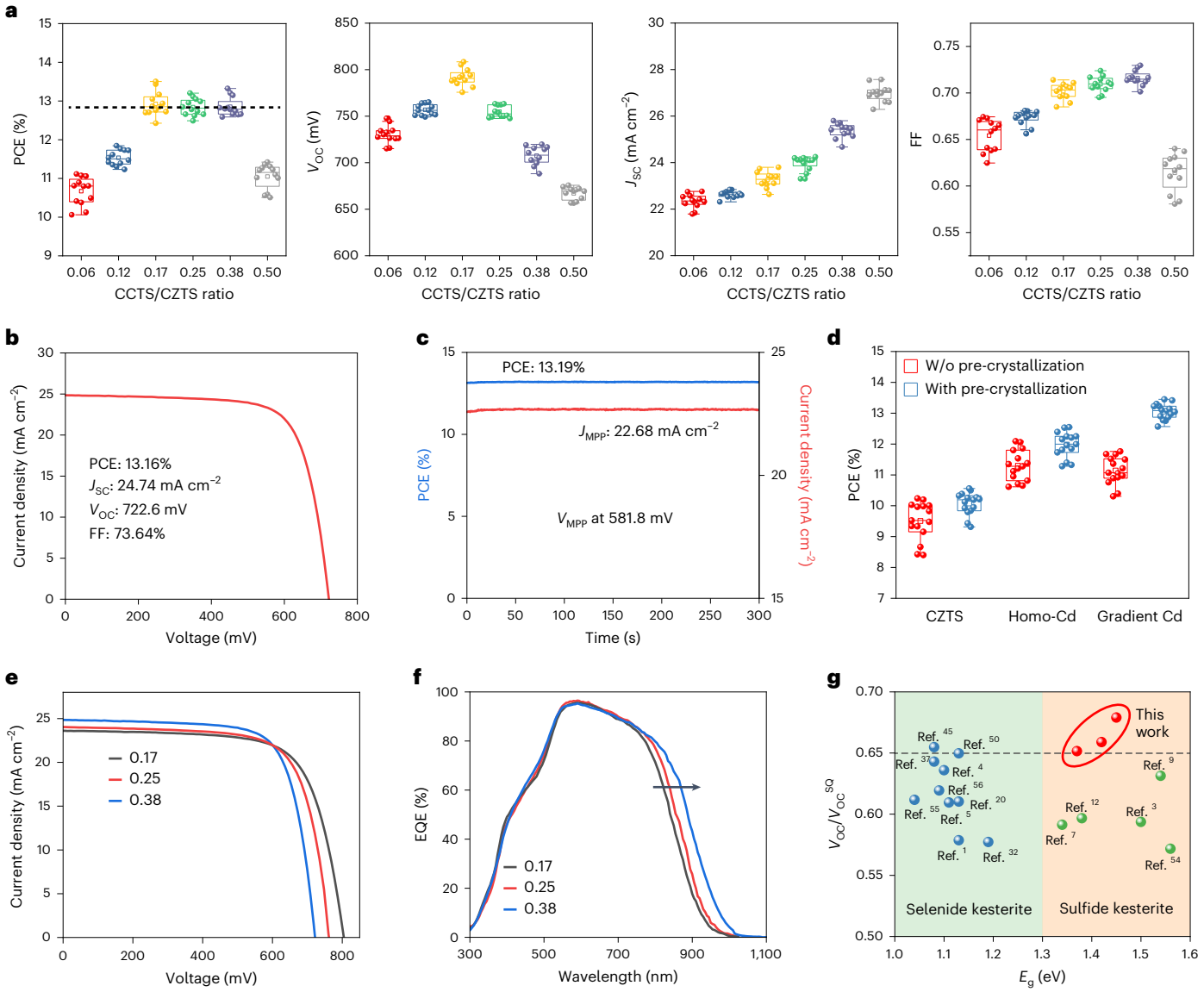

Fig. 4 | Performance of photovoltaic devices. a, Performance parameters (PCE, V_{OC},J_{SC} and FF) of GCd-CZTS devices with different CCTS/CZTS ratios fabricated in one batch (n = 12 per group). The dashed line is guidance for the eyes. **b**,**c**, Certified current–voltage curve (**b**) and steady-state output performance (**c**) of a GCd-CZTS device fabricated with a CCTS/CCTS ratio of 0.38. The current-voltage curve showed the cell has PCE of 13.16% with J_{SC} of 24.74 mA cm^{-2}, V_{OC} of 722.6 mV and FF of 0.736. The steady-state output demonstrated PCE of 13.19% for the cell working in the maximum power point at 581.8 mV (V_{MPP}) with current density output of 22.68 mA cm^{-2} (J_{MPP}). **d**, PCEs of cells using different Cd alloying strategies, including non-alloying, homogeneous alloying (Homo-Cd) and gradient-Cd alloying, with (blue) or without pre-crystallization (red) (n = 15 per group). **e**,**f**, Current–voltage curves (**e**) and EQE spectra (**f**) of cells fabricated with different CCTS/CCTS ratios (0.17, 0.25 and 0.38). In **e**, these respective cells had J_{SC} values of 23.6, 24.1 and 24.7 mA cm^{-2}, V_{OC} values of 805, 762 and 723 mV, FF values of 0.71, 0.72 and 0.74 and PCE values of 13.5, 13.2 and 13.2%. In **f**, bandgaps (E_g = 1.45, 1.42 and 1.37 eV, respectively) were derived from the maximum position of the derivative of the EQE. The corresponding J_{SC} values were 25.1, 26.0 and 27.1 mA cm^{-2}, respectively. **g**, A summary of V_{OC}/V_{OC}^{SQ} values of representative kesterite solar cells that have been reported previously[1,3–5,7,9,12,20,32,37,45,50,54–56]. Detailed data are provided in Supplementary Table 1. The dashed line is guidance for the eyes. In **a** and **d**, the central lines represent median values, the box limits represent the upper and lower quartiles, the whiskers represent the maximum and minimum and the raw data points are also displayed. Credit: **b**,**c**, NPVM.

reduce the limitation of organic frameworks on the growth of kesterite crystals and could promote crystallization of the bottom region of the film, avoiding the appearance of fine grains. The application of this strategy in the selenide kesterite film is expected to realize more significant cell efficiency breakthroughs.

As has been accomplished for CIGS[26,27], the gradient elemental composition and band structure in kesterite solar cells need to be further explored and optimized; for example, by discovering more appropriate alloying elements that have energy band regulation ability and relatively low migration ability, enhancing the composition gradient in the middle and bottom regions of the absorber to increase the conduction band bending, constructing a front gradient to further reduce interfacial recombination. In this process, the regulation of crystal growth and element diffusion kinetics through the pre-crystallization strategy will continue to play an important role. To more precisely achieve this promising crystallization regulation, the mechanisms of complex chemical reactions occurring during precursor film preparation, pre-crystallization and sulfurization/selenization processes need to be further revealed. These primarily include transformation from metal–organic coordination complexes and excessive organic additives or solvents to metal sulfides or oxides and other organic components under annealing, as well as the molecular or

atomic structure evolution of these compounds at high temperature under a reactive atmosphere, such as H_2S, S or Se.

Conclusion

In this study, we have developed a gradient energy band structure within a Cd-alloyed CZTS absorber to facilitate bulk carrier transport for the purpose of reducing the charge and V_{OC} loss of the sulfide kesterite solar cell. In particular, we explored a pre-crystallization strategy that overcomes a persistent challenge in the construction of a gradient bandgap in CZTS films: namely, the rapid diffusion of elements. Specifically, this strategy achieved uniform synchronous nucleation and crystallization at different spatial locations of the absorber film and improved the crystal quality, thereby significantly slowing down Zn/Cd element interdiffusion during the high-temperature sulfurization reaction process and realizing a gradient element distribution in the absorber. The Zn/Cd distribution introduced an obvious gradient in the conduction band of the absorber, which on one hand significantly facilitated the bulk carrier transfer and on the other hand improved the energy band alignment and reduced defects at the heterojunction interface. As a result, the Cd-gradient CZTS solar cell demonstrates a high certified total-area efficiency of 13.16%, with significant voltage loss reduction compared with previous results, thus representing a substantial step forward for the pure-sulfide kesterite solar cell.

Methods

Materials

CuCl (99.999%; Alfa Aesar), $Zn(CH_3COO)_2$ (99.99%; Aladdin Scientific), $Cd(CH_3COO)_2$ (99.995%; Macklin), $SnCl_4$ (99.998%; Macklin), thiourea (99.99%; Aladdin Scientific (recrystallized twice)), 2-methoxyethanol (99.8%; Aladdin Scientific), sulfur powder (99.99%; ZhongNuo Advanced Material), $CdSO_4{\cdot}8/3H_2O$ (99.99%; Aladdin Scientific), ammonium chloride (≥99.5%; Sinopharm Chemical Reagent) and ammonium hydroxide (~25.0–28.0%; Sinopharm Chemical Reagent) were used to prepare the precursor solution and CdS. These chemicals were used directly without further purification.

Film fabrication

The CZTS and CCTS precursor solution was prepared as follows: CuCl, $Zn(CH_3COO)_2$ or $Cd(CH_3COO)_2$ plus $SnCl_4$ and thiourea were dissolved in 2-methoxyethanol and stirred at 60 °C for 1 h to obtain a colourless solution. The molar ratios of Cu/(Zn(Cd) + Sn), Zn(Cd)/Sn and thiourea/metal were 0.85, 1.20 and 1.95, respectively, and the concentrations of metal elements and thiourea were 1.63 and 3.18 mol l^{-1}. The CZTS/CCTS precursor films were prepared by subsequently spin-coating the CZTS/CCTS precursor solution on cleared Mo substrates at a spin speed of 3,000 r.p.m. s^{-1} for 25 s, followed by annealing on a 280 °C hot plate in the air. The coating and annealing processes were repeated several times for the desired 1.2- to 1.5-μm-thickness precursor films. Then, as-prepared precursor films were first annealed with H_2S (10%)/Ar_2 flow at 420 °C for 10 min using a rapid thermal processor (AS-One 100) and then annealed with N_2 flow in a sulfur-contained graphite box, which was put inside a heating tube furnace. The temperature was raised to 580 °C within 40 min, held for 20 min and finally naturally cooled. For the absorber with cells based on homogeneous Cd alloying, the Cd source was directedly added to the CZTS precursor solution and the film deposition adopted the same procedures as those described above.

Device fabrication

A device structure with Mo, kesterite, CdS, ZnO, indium tin oxide, Ni/Al and MgF_2 was fabricated successively by adding together a kesterite absorber layer, a chemical-bath-deposited CdS buffer layer (40–50 nm; after which followed a heterojunction heat treatment at 280 °C for 7 min under a nitrogen atmosphere), a radio frequency magnetron-sputtered intrinsic ZnO (20–30 nm) layer combined with indium tin oxide window layers (180–200 nm), a thermally evaporated Ni/Al collection grid (2 μm) and an MgF_2 anti-reflection layer (100 nm). The cells were separated from each other by mechanical scribing. The measuring active area was around 0.2212 cm^2 (without the grid line). The certified mask area was determined by the National PV Industry Measurement and Testing Center to be 0.2311 cm^2.

Film characterization

Raman spectra were collected using a Raman spectrometer (LabRAM HR Evolution; HORIBA) with a 532 or 325 nm excitation laser. Scanning electron microscopy images were taken with a scanning electron microscope (Sigma 300) under 10 kV at various magnifications. Element maps were obtained using an energy-dispersive spectrometer (AZtec X-Max 50). The total film compositions were determined using an energy-dispersive X-ray fluorescence spectrometer (EDX-7000; Shimadzu). The transmission electron microscopy specimens were made using a focused ion beam with a micro-sampling system (FEI xT Nova 200 NanoLab). STEM images were obtained with a transmission electron microscope (ARM200F; JEOL) equipped with a Gatan Quantum ER965 imaging filter operating at 200 kV. The noisy contrast of the acquired images was removed using a Wiener filter. Inverse photoelectron spectroscopy and UPS were performed on a multifunctional photoelectron spectrometer (Axis Ultra DLD). Transient photoluminescence was measured on a photoluminescence spectrometer (FLS 900) following excitation with a picosecond-pulsed diode laser (EPL-640) of 638.2 nm wavelength and cooling down with liquid helium. KPFM images were obtained on a Bruker MultiMode 9 system.

Device characterization

The *C*–*V* profiles, drive-level capacitance profiling and temperature-dependent *I*–*V* profiles were measured on an electrochemical workstation (VersaSTAT; Princeton Applied Research). Modulated electrical transient spectra were obtained by our laboratory-made setup, in which the cell was excited by a 640 nm nanosecond pulse laser and the photovoltage decay process was recorded by a digital oscilloscope (DPO7104; Tektronix). The current–voltage characteristics of the cells were recorded using a Keithley 2601 Source Meter under simulated AM 1.5 G sunlight (100 mW cm^{-2}) calibrated with an Si reference cell (calibrated by the National Institute of Metrology of China). The voltage was scanned from −50 to 850 or 800 mV and the scanning rate was about 90 mV s^{-1}. All of the measurements were performed under ambient conditions (air, 25 °C and uncontrolled humidity) and no preconditioning was applied before the measurements. EQE spectra were measured with an Enlitech QE-R system with calibrated Si and Ge diodes as references. Thermal admittance spectra were recorded using an electrochemical workstation (VersaSTAT3, Princeton Applied Research) in the dark and the cell temperature was controlled using a low-temperature probe station (TTPX; Lakeshore).

DFT calculation

All of the calculations were carried out under the scheme of spin-polarized DFT using CASTEP[51]. Specifically, the Perdew–Burke–Ernzerhof exchange correlation functional within the generalized gradient approximation was employed to describe the exchange correlation energy[52]. Geometric convergence tolerances were set for maximum force of 0.03 eV $Å^{-1}$, with a maximum energy change of 10^{-5} eV per atom, a maximum displacement of 0.001 Å and maximum stress of 0.05 GPa. The plane wave energy cut-off was set at 600 eV and the sampling in the Brillouin zone was set to 3 × 3 × 1 using the Monkhorst–Pack method. The diffusion of Zn/Cd was investigated by searching the possible diffusion route and identifying the migration transition state with the lowest diffusion energy barrier. The diffusion energy barrier was calculated as the energy difference between the total energies of the transition state and the initial structure. The transition state was searched using the generalized synchronous transit

(linear synchronous transit (LST)/quadratic synchronous transit (QST)) method implemented using CASTEP code[53]. The algorithm starts from an LST optimization and continues with a QST maximization process. Thereafter, conjugate gradient minimization is conducted from the obtained LST/QST structure to refine the geometry of the transition state. The LST, QST and conjugate gradient calculations are repeated until a stable transition state is obtained.

Reporting summary

Further information on research design is available in the Nature Portfolio Reporting Summary linked to this article.

Data availability

The main data supporting the findings of this study are available within the main text, Supplementary Information and Supplementary Data 1. Source data are provided with this paper.

References

1. Wang, W. et al. Device characteristics of CZTSSe thin-film solar cells with 12.6% efficiency. *Adv. Energy Mater.* **4**, 1301465 (2014).
2. Antunez, P. D., Bishop, D. M., Luo, Y. & Haight, R. Efficient kesterite solar cells with high open-circuit voltage for applications in powering distributed devices. *Nat. Energy* **2**, 884–890 (2017).
3. Yan, C. et al. Cu_2ZnSnS_4 solar cells with over 10% power conversion efficiency enabled by heterojunction heat treatment. *Nat. Energy* **3**, 764–772 (2018).
4. Zhou, J. et al. Control of the phase evolution of kesterite by tuning of the selenium partial pressure for solar cells with 13.8% certified efficiency. *Nat. Energy* **8**, 526–535 (2023).
5. Gong, Y. et al. Elemental de-mixing-induced epitaxial kesterite/CdS interface enabling 13%-efficiency kesterite solar cells. *Nat. Energy* **7**, 966–977 (2022).
6. Best research-cell efficiency chart. *NREL* https://www.nrel.gov/pv/cell-efficiency.html
7. Su, Z. et al. Device postannealing enabling over 12% efficient solution-processed Cu_2ZnSnS_4 solar cells with Cd^{2+} substitution. *Adv. Mater.* **32**, e2000121 (2020).
8. Yan, C. et al. Beyond 11% efficient sulfide kesterite $Cu_2Zn_xCd_{1-x}SnS_4$ solar cell: effects of cadmium alloying. *ACS Energy Lett.* **2**, 930–936 (2017).
9. Wang, A. et al. Cd-free pure sulfide kesterite Cu_2ZnSnS_4 solar cell with over 800 mV open-circuit voltage enabled by phase evolution intervention. *Adv. Mater.* **36**, e2307733 (2024).
10. Hadke, S. H. et al. Synergistic effects of double cation substitution in solution-processed CZTS solar cells with over 10% efficiency. *Adv. Energy Mater.* **8**, 1802540 (2018).
11. Kauk-Kuusik, M. et al. Cu_2ZnSnS_4 monograin layer solar cells for flexible photovoltaic applications. *J. Mater. Chem. A* **11**, 23640–23652 (2023).
12. Pan, X. et al. 12.3% Efficient low V_{OC} loss pure sulfide kesterite solar cells from DMSO solution via cadmium alloying. *Adv. Funct. Mater.* **13**, 2301780 (2023).
13. Green, M. A. et al. Solar cell efficiency tables (version 63). *Prog. Photovolt. Res. Appl.* **32**, 3–13 (2023).
14. Gong, Y. et al. Identifying the origin of the V_{OC} deficit of kesterite solar cells from the two grain growth mechanisms induced by Sn^{2+} and Sn^{4+} precursors in DMSO solution. *Energy Environ. Sci.* **14**, 2369–2380 (2021).
15. Chen, W., Dahliah, D., Rignanese, G. M. & Hautier, G. Origin of the low conversion efficiency in Cu_2ZnSnS_4 kesterite solar cells: the actual role of cation disorder. *Energy Environ. Sci.* **14**, 3567–3578 (2021).
16. Kim, S., Park, J.-S., Hood, S. N. & Walsh, A. Lone-pair effect on carrier capture in Cu_2ZnSnS_4 solar cells. *J. Mater. Chem. A* **7**, 2686–2693 (2019).
17. Li, J. et al. Unveiling microscopic carrier loss mechanisms in 12% efficient $Cu_2ZnSnSe_4$ solar cells. *Nat. Energy* **7**, 754–764 (2022).
18. Kim, S., Márquez, J. A., Unold, T. & Walsh, A. Upper limit to the photovoltaic efficiency of imperfect crystals from first principles. *Energy Environ. Sci.* **13**, 1481–1491 (2020).
19. Monserrat, B., Park, J.-S., Kim, S. & Walsh, A. Role of electron–phonon coupling and thermal expansion on band gaps, carrier mobility, and interfacial offsets in kesterite thin-film solar cells. *Appl. Phys. Lett.* **112**, 193903 (2018).
20. Persson, C. Electronic and optical properties of Cu_2ZnSnS_4 and $Cu_2ZnSnSe_4$. *J. Appl. Phys.* **107**, 053710 (2010).
21. Duan, B. W. et al. Underlying mechanism of the efficiency loss in CZTSSe solar cells: disorder and deep defects. *Sci. China Mater.* **63**, 2371–2396 (2020).
22. Ramkumar, S. P. et al. Insights into cation disorder and phase transitions in CZTS from a first-principles approach. *Phys. Rev. Mater.* **2**, 085403 (2018).
23. Bourdais, S. et al. Is the Cu/Zn disorder the main culprit for the voltage deficit in kesterite solar cells? *Adv. Funct. Mater.* **6**, 1502276 (2016).
24. Larsen, J. K., Scragg, J. J. S., Ross, N. & Platzer-Björkman, C. Band tails and Cu–Zn disorder in Cu_2ZnSnS_4 solar cells. *ACS Appl. Energy Mater.* **3**, 7520–7526 (2020).
25. Gokmen, T., Gunawan, O., Todorov, T. K. & Mitzi, D. B. Band tailing and efficiency limitation in kesterite solar cells. *Appl. Phys. Lett.* **103**, 103506 (2013).
26. Chirilă, A. et al. Highly efficient $Cu(In,Ga)Se_2$ solar cells grown on flexible polymer films. *Nat. Mater.* **10**, 857–861 (2011).
27. Kato, T. $Cu(In,Ga)(Se,S)_2$ solar cell research in Solar Frontier: progress and current status. *Jpn J. Appl. Phys.* **56**, 04ca02 (2017).
28. Keller, J. et al. High-concentration silver alloying and steep back-contact gallium grading enabling copper indium gallium selenide solar cell with 23.6% efficiency. *Nat. Energy* **9**, 467–478 (2024).
29. Qi, Y. et al. Engineering of interface band bending and defects elimination via a Ag-graded active layer for efficient $(Cu,Ag)_2ZnSn(S,Se)_4$ solar cells. *Energy Environ. Sci.* **10**, 2401–2410 (2017).
30. Yuan, Z. et al. Engineering solar cell absorbers by exploring the band alignment and defect disparity: the case of Cu- and Ag-based kesterite compounds. *Adv. Funct. Mater.* **25**, 6733–6743 (2015).
31. Yang, K. et al. A band-gap-graded CZTSSe solar cell with 12.3% efficiency. *J. Mater. Chem. A* **4**, 10151–10158 (2016).
32. Zhao, Y. et al. Controllable double gradient bandgap strategy enables high efficiency solution-processed kesterite solar cells. *Adv. Funct. Mater.* **34**, 2311992 (2023).
33. Son, D.-H. et al. Effect of solid-H_2S gas reactions on CZTSSe thin film growth and photovoltaic properties of a 12.62% efficiency device. *J. Mater. Chem. A* **7**, 25279–25289 (2019).
34. Xu, X. et al. Controlling selenization equilibrium enables high-quality kesterite absorbers for efficient solar cells. *Nat. Commun.* **14**, 6650 (2023).
35. Mangan, T. C., McCandless, B. E., Dobson, K. D. & Birkmire, R. W. Thermochemical and kinetic aspects of $Cu_2ZnSn(S,Se)_4$ thin film growth by reacting Cu–Zn–Sn precursors in H_2S and H_2Se. *J. Appl. Phys.* **118**, 065303 (2015).
36. Guo, H. et al. Band-gap-graded $Cu_2ZnSn(S,Se)_4$ drives highly efficient solar cells. *Energy Environ. Sci.* **15**, 693–704 (2022).
37. Gong, Y. et al. Ag incorporation with controlled grain growth enables 12.5% efficient kesterite solar cell with open circuit voltage reached 64.2% Shockley–Queisser limit. *Adv. Funct. Mater.* **31**, 2101927 (2021).

38. Su, Z. et al. Cation substitution of solution-processed Cu_2ZnSnS_4 thin film solar cell with over 9% efficiency. *Adv. Funct. Mater.* **5**, 1500682 (2015).
39. Xiao, Z. et al. Bandgap engineering of $Cu_2Cd_xZn_{1-x}SnS_4$ alloy for photovoltaic applications: a complementary experimental and first-principles study. *J. Appl. Phys.* **114**, 183506 (2013).
40. Pilvet, M. et al. Compositionally tunable structure and optical properties of $Cu_{1.85}(Cd_xZn_{1-x})_{1.1}SnS_{4.1}$ ($0 \le x \le 1$) monograin powders. *Thin Solid Films* **582**, 180–183 (2015).
41. Fan, P. et al. Over 10% efficient Cu_2CdSnS_4 solar cells fabricated from optimized sulfurization. *Adv. Funct. Mater.* **32**, 2207470 (2022).
42. Hadke, S. et al. Suppressed deep traps and bandgap fluctuations in Cu_2CdSnS_4 solar cells with ≈8% efficiency. *Adv. Energy Mater.* **9**, 1902509 (2019).
43. Shi, J. et al. Identification of high-temperature exciton states and their phase-dependent trapping behaviour in lead halide perovskites. *Energy Environ. Sci.* **11**, 1460–1469 (2018).
44. Heath, J. T., Cohen, J. D. & Shafarman, W. N. Bulk and metastable defects in $CuIn_{1-x}Ga_xSe_2$ thin films using drive-level capacitance profiling. *J. Appl. Phys.* **95**, 1000–1010 (2004).
45. Shi, J. et al. Multinary alloying for facilitated cation exchange and suppressed defect formation in kesterite solar cells with above 14% certified efficiency. *Nat. Energy* **9**, 1095–1104 (2024).
46. Gunawan, O., Todorov, T. K. & Mitzi, D. B. Loss mechanisms in hydrazine-processed $Cu_2ZnSn(Se,S)_4$ solar cells. *Appl. Phys. Lett.* **97**, 233506 (2010).
47. Li, Y. et al. Exploiting electrical transients to quantify charge loss in solar cells. *Joule* **4**, 472–489 (2020).
48. Shi, J. et al. From ultrafast to ultraslow: charge-carrier dynamics of perovskite solar cells. *Joule* **2**, 879–901 (2018).
49. Larsen, J. K. et al. Cadmium free Cu_2ZnSnS_4 solar cells with 9.7% efficiency. *Adv. Energy Mater.* **9**, 1900439 (2019).
50. Li, Y. et al. Suppressing element inhomogeneity enables 14.9% efficiency CZTSSe solar cells. *Adv. Mater.* **36**, 2400138 (2024).
51. Clark, S. J. et al. First principles methods using CASTEP. *Z. Kristallogr.* **220**, 567–570 (2005).
52. Perdew, J. P., Burke, K. & Ernzerhof, M. Generalized gradient approximation made simple. *Phys. Rev. Lett.* **77**, 3865–3868 (1996).
53. Govind, N., Petersen, M., Fitzgerald, G., King-Smith, D. & Andzelm, J. A generalized synchronous transit method for transition state location. *Comp. Mater. Sci.* **28**, 250–258 (2003).
54. Cui, X. et al. Cd-free Cu_2ZnSnS_4 solar cell with an efficiency greater than 10% enabled by Al_2O_3 passivation layers. *Energy Environ. Sci.* **12**, 2751–2764 (2019).
55. Li, J. et al. Defect control for 12.5% efficiency $Cu_2ZnSnSe_4$ kesterite thin-film solar cells by engineering of local chemical environment. *Adv. Mater.* **32**, 2005268 (2020).
56. Sun, Y. et al. N-type surface design for p-type CZTSSe thin film to attain high efficiency. *Adv. Mater.* **33**, 2104330 (2021).

Acknowledgements

We thank W. Wang of Institute of Physics, Chinese Academy of Sciences for STEM support and Z. Su from Shenzhen University for valuable discussions and insightful suggestions. This work was supported by the National Natural Science Foundation of China (grants 52222212 (to J.S.), U2002216 (to Q.M.), 52227803 (to Q.M.) and 52172261 (to Y.L.)). J.S. also gratefully acknowledges support from the Youth Innovation Promotion Association of the Chinese Academy of Sciences (2022006).

Author contributions

K.Y., J.S., Y.L. and Q.M. conceived of the idea and designed the experiments. K.Y., J.W. and L.L. performed the experiments and data analysis. F.M. performed the transmission electron microscopy characterization and analysis. L.L., X.X., B.Z. and M.J. supported the CZTS solar cell fabrication. H.W. and D.L. contributed to the discussion. K.Y., J.S., Y.L. and Q.M. participated in writing the manuscript.

Competing interests

The authors declare no competing interests.

Additional information

Supplementary information The online version contains supplementary material available at https://doi.org/10.1038/s41560-024-01681-w.

Correspondence and requests for materials should be addressed to Jiangjian Shi, Yanhong Luo or Qingbo Meng.

Peer review information *Nature Energy* thanks the anonymous reviewers for their contribution to the peer review of this work.

Corresponding author(s): JIANGJIAN SHI, YANHONG LUO, QINGBO MENG

Solar Cells Reporting Summary

Nature Portfolio wishes to improve the reproducibility of the work that we publish. This form is intended for publication with all accepted papers reporting the characterization of photovoltaic devices and provides structure for consistency and transparency in reporting. Some list items might not apply to an individual manuscript, but all fields must be completed for clarity.

For further information on Nature Research policies, including our data availability policy, see Authors & Referees.

Experimental design

Please check the following details are reported in the manuscript, and provide a brief description or explanation where applicable.

1. Dimensions

Area of the tested solar cells	☒ Yes	The area is 0.2311 cm2 and it is given in the certification report.
	☐ No	*Explain why this information is not reported/not relevant.*
Method used to determine the device area	☒ Yes	The device area is determined by mask
	☐ No	*Explain why this information is not reported/not relevant.*

2. Current-voltage characterization

Current density-voltage (J-V) plots in both forward and backward direction	☒ Yes	The forward and backward scan J-V curves are given in certification report and it shows no hysteresis.
	☐ No	
Voltage scan conditions	☒ Yes	The voltage was scanned from -50 mV to 850 or 800 mV with a scanning rate of 90 mV·s-1 and it is given in experimental section.
	☐ No	*Explain why this information is not reported/not relevant.*
Test environment	☒ Yes	The J-V tests were conducted in air at 25 °C. The test environment is given in experimental section.
	☐ No	*Explain why this information is not reported/not relevant.*
Protocol for preconditioning of the device before its characterization	☒ Yes	No preconditioning of the device was before the measurement. This is given in experimental section.
	☐ No	*Explain why this information is not reported/not relevant.*
Stability of the J-V characteristic	☒ Yes	Kesterite solar cells do not have hysteresis . In the certification process, maximum power output had been traced for five minutes to confirm the cell efficiency, as given in fig 4.
	☐ No	*Explain why this information is not reported/not relevant.*

3. Hysteresis or any other unusual behaviour

Description of the unusual behaviour observed during the characterization	☐ Yes	*Provide a description of hysteresis or any other unusual behaviour observed during the characterization.*
	☒ No	Kesterite solar cells do not have hysteresis or other unusual behaviour.
Related experimental data	☐ Yes	*Provide a description of the related experimental data.*
	☒ No	Kesterite solar cells do not have hysteresis or other unusual behaviour.

4. Efficiency

External quantum efficiency (EQE) or incident photons to current efficiency (IPCE)	☒ Yes	EQE is given in Figure 4.
	☐ No	*Explain why this information is not reported/not relevant.*
A comparison between the integrated response under the standard reference spectrum and the response measure under the simulator	☒ Yes	Given in Figure 4.
	☐ No	*Explain why this information is not reported/not relevant.*

For tandem solar cells, the bias illumination and bias voltage used for each subcell

☐ Yes
☒ No

Provide a description of the measurement conditions.

No tandem solar cell was studied.

5. Calibration

Light source and reference cell or sensor used for the characterization

☒ Yes
☐ No

The current–voltage characteristics of the cells were recorded by a Keithley 2601 Source Meter under simulated AM 1.5G sunlight (100 mW cm-2) calibrated with a Si reference cell (calibrated by the National Institute of Metrology of China). This is given in experimental section.

Explain why this information is not reported/not relevant.

Confirmation that the reference cell was calibrated and certified

☒ Yes
☐ No

The reference cell was calibrated by National Institute of Metrology, China. This is given in experimental section.

Explain why this information is not reported/not relevant.

Calculation of spectral mismatch between the reference cell and the devices under test

☒ Yes
☐ No

The mismatch factor is 1.016 and this is given in certification report.

Explain why this information is not reported/not relevant.

6. Mask/aperture

Size of the mask/aperture used during testing

☒ Yes
☐ No

The mask area is 0.2311 cm2 and this is given in certification report.

Explain why this information is not reported/not relevant.

Variation of the measured short-circuit current density with the mask/aperture area

☐ Yes
☒ No

Report the difference in the short-circuit current density values measured with the mask and aperture area.

No such phenomenon in kesterite solar cells and our test area is large enough to avoid this effect.

7. Performance certification

Identity of the independent certification laboratory that confirmed the photovoltaic performance

☒ Yes
☐ No

The photovoltaic performance is certified in NPVM, as given in the supplementary information.

Explain why this information is not reported/not relevant.

A copy of any certificate(s)

☒ Yes
☐ No

The certification report is given in supplementary information

Explain why this information is not reported/not relevant.

8. Statistics

Number of solar cells tested

☒ Yes
☐ No

The exact number of cells is given in the figure caption of each statistical analysis.

Explain why this information is not reported/not relevant.

Statistical analysis of the device performance

☒ Yes
☐ No

Statistical analysis of the device performance is given in figure 4 and supplementary information.

Explain why this information is not reported/not relevant.

9. Long-term stability analysis

Type of analysis, bias conditions and environmental conditions

☐ Yes
☒ No

Provide a description of the type of analysis, bias conditions and environmental conditions (e.g. illumination type, temperature, atmosphere humidity, encapsulation method, preconditioning temperature, bias) for each long-term stability analysis carried out; see ref. 7 and 8 for details.

No stability problem has been reported in kesterite solar cells